Journal of Physics: Conference Series

PAPER • OPEN ACCESS

Wake meandering and its relationship with the incoming wind characteristics: a statistical approach applied to long-term on-field observations

To cite this article: E. Torres Garcia *et al* 2017 *J. Phys.: Conf. Ser.* **854** 012045

IOP Conf. Series: Journal of Physics: Conf. Series **854** (2017) 012045 doi:10.1088/1742-6596/854/1/012045

Wake meandering and its relationship with the incoming wind characteristics: a statistical approach applied to long-term on-field observations

E. Torres Garcia[1*], S. Aubrun[1], M. Boquet[2], P. Royer[2], O. Coupiac[3] and N. Girard[3]

1 Univ. Orleans, PRISME EA4229, 45072 Orleans, France

2 Leosphere, Jean Rostand 14-16, 91400 Orsay, France

3 Maia Eolis, Tour de Lille, Bvd de Turin 59777 Lille, France

*eulalio.torres-garcia@univ-orleans.fr

Abstract. In several papers, the importance of the atmospheric flow in the wake development of wind turbines (WT) has been pointed out, making it clear that it is necessary to have long-term on-field observations for an appropriate description of the wake development, its structure and dynamics. This work presents a statistical approach to wake meandering, y_ω, and the relationship that this behavior has with the incoming wind conditions and neighboring wakes. The work was developed in the framework of the French project SMARTEOLE. The study is based on a 7-month measurement campaign in which a pulsed scanning LiDAR system was used. The ground based LiDAR, measures the flow field in a segment such that the wake of two wind turbines can be captured quasi-horizontally. The analysis filters the incoming wind conditions according to the thermal stability, wind direction and wind velocity at hub height; therefore, the wakes that are developed in periods with similar wind conditions are expected to be analogous, hence meandering can be tracked and statistically analyzed. A well-defined wake evolution was found and the uncertainty analysis made on the wake meandering uncovered some interesting characteristics, including the number of samples required to reach a statistical uncertainty on the mean wake position between 2×10^{-2} D and 8×10^{-2} D for a confidence interval of 95%.

1. Introduction

In wind farms (WFs), some of the undesired effects of wind turbine (WT) wakes are power losses and a decrease in the lifetime of structures embedded within the wakes [1]. Many simulation tools, numerical [2–5] and experimental [6,7], focus on the wake's development in order to better understand the wake physics and reduce such undesired effects; the final objective is to design efficient wind farm layouts. The problem arises when the physics exceeds the simulation tool limitations, i.e. for numerical simulations the number of operations is beyond current calculation capabilities and for experimental simulation, the changing environmental variables make it impossible to simulate them all. As a result, from a wind farm design to its operation, there is a power output difference of up to 20% (mostly negative) [8]. Detailed observations of the atmospheric flow and its interaction with operational WTs (upwind and downwind) are required to calibrate numerical models and corroborate wind tunnel experiments.

When doing field measurements, the expected outcome is the understanding of the complex atmospheric flow field behavior, which in turn generates a rule that can be extended to any real case (see [9–11] for some studies dealing with wakes in on-field measurements). The problem to generate such outcome is the atmospheric stability, which depends on variables such as mean wind velocity ($\bar{U}$), mean wind direction (*WD*), Monin-Obukhov Length (L) and turbulence intensity (I_u). Moreover, the wake topology is related to many other aspects such: wind farm layout, landscape and neighboring wakes [11], that make it a hard target to describe. Detailed observations over long periods will help to understand the synergy between atmospheric flow and wakes, to characterize the impact of the wakes on other wind turbines and also, as Rhodes et al. [12] suggested, the impact on the local environment.

One of the promising measuring techniques to characterize WT wakes is Light Detection and Ranging (LiDAR) sensors. LiDAR remotely senses the Doppler shift of laser light backscattered from particles carried by the wind in order to measure a line-of-sight (LOS) radial wind velocity. The system considers measurements of this LOS velocity in multiple radial directions in order to estimate wind characteristics [13]. LiDARs have been used to estimate wind characteristics of boundary layer dynamics [14,15] and also for wake dynamics [12,16].

In the present study a LiDAR measurement campaign, lasting 7 months, is analyzed. The objective was to analyze the unsteady wake behavior of two wind turbines. The measurements were performed by a ground based scanning LiDAR WINDCUBE 200S. The LiDAR was programmed to acquire 30 LOS to form a plane at a specific elevation angle; three elevation angles were programmed. Details of the LiDAR and experimental set up are presented in section 2. In order to analyze the wake physics, each plane was treated individually, assuming conditions of homogenous flow along the plane and also assuming that the turbulent structures move as frozen entities transported by the mean wind [17]. The methods used to categorize measurements and the methods to analyze the categories are presented in section 3. The unsteady wake behavior was assessed statistically, the outcome of the statistical analysis and the discussion are presented in section 4. Finally, conclusions are drawn in section 5.

2. Experimental set up

The measurement campaign took place between 15/11/2015 and 30/05/2016. More than 4300 hours of measurements were collected and analyzed.

2.1. The wind farm

The WF belongs to Maïa Eolis (Engie Green) and it is located in the north of France, on the western limit of the municipality of Ablaincourt-Pressoir, see Figure 1. The WF is composed of seven SENVION MM82 wind turbines, whose diameter (D) and hub height are 82 m and 80 m, respectively. The turbines are sited from north to south and spaced approximately 3.5 D apart. The WTs are named SMV1 to SMV7, SMV1 being the northernmost; for a detailed description see [18]. The measurement campaign focused on SMV5 and SMV6; these turbines are aligned to a 207° reference line (orientated in meteorological coordinates).

2.2. The instrumentation

A pulsed scanning LiDAR WINDCUBE 200S, provided by LEOSPHERE, was located at ground level on the outskirts of Ablaincourt-Pressoir (see B, in Figure 1 right); this location is 1320 m east from the line of WTs. The system has a velocity accuracy of 0.1 $m \cdot s^{-1}$ [19] and was programmed to acquire 115 measurement points along a line of sight (LOS). 30 LOSs form a plane position indicator (PPI). Each PPI was measured between azimuth 243° and 273° with respect to the geographical north and in meteorological coordinates (see C, in Figure 1 right). The acquisition resolution along each LOS is 25 m and the displacement between LOS is 1° at $2° \cdot s^{-1}$ acquisition rate, therefore a full PPI is obtained every 15 s. The LiDAR was programmed to acquire PPIs at three elevation angles: α_1=2.5°, α_2=3.8° and α_3=5.2°, with respect to the ground level. The selection of azimuths and elevations for acquiring measurements was based on the geographical location of the turbines, their geometrical parameters and the historical wind rose; hence, SMV5 and SMV6 wakes were captured within the specified PPIs. In addition, because of the location of the LiDAR and the selected elevation angles, the PPIs crossed SMV5 at heights of 58 m for α_1, 79 m for α_2 and 120 m for α_3.

An 80 m high lattice met mast is located 1.6 km northeast of SMV6, see A in Figure 1. An 80 m anemometer and a 40 m wind vane were operational throughout the measurement campaign.

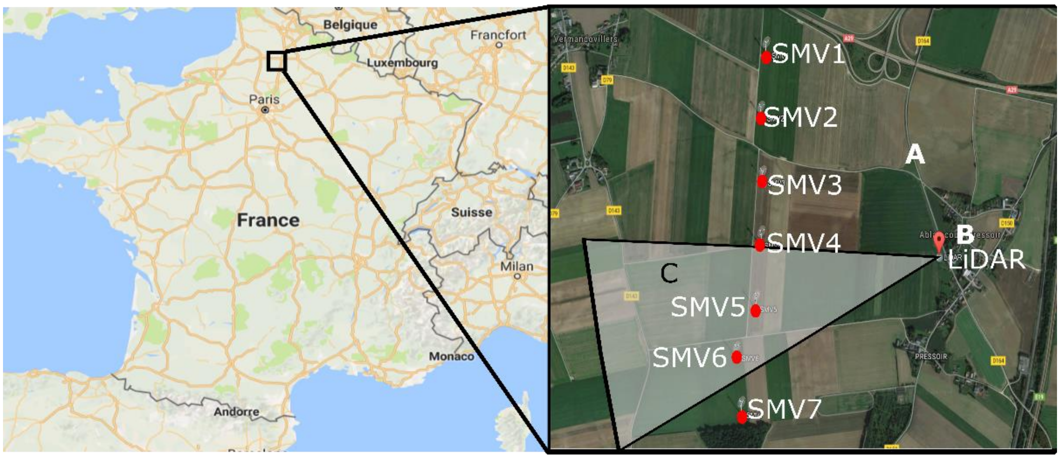

Figure 1. Map of France indicating the wind farm site (left). On the right, the wind farm composed of seven WTs marked with red dots. A meteorological mast (A) is located in the surrounding area. The location of the LiDAR is marked with a B. The shadowed area C is the LiDAR scanned area.

2.3. External resources

The Modern-Era Retrospective analysis for Research and Applications version 2 (MERRA-2) dataset is a global reanalysis to assimilate space-based observations of aerosols and represent their interactions with other physical processes in the climate system [20]. The MERRA-2 spatial resolution is 1/2° (latitude) and 2/3° (longitude) and the temporal resolution is 1 hour. MERRA-2 has proven to be a valuable dataset for the determination of the overall stability conditions of a site, as long as the surrounding grid points are representative for the site [21]. The data were extracted from the closest MERRA-2 grid point located 2.5 E- 49.5 N, 44 km South West from the wind farm. The MERRA-2 data provide information about wind direction, wind velocity, pressure and temperature. The Monin-Obukhov Length (L) can be calculated from MERRA-2 [21].

3. Methods

In order to ensure the right statistical description the atmospheric wind conditions were filtered. The three filter criteria applied were: 1) Neutral atmosphere corresponding to $|L| \geq 1000$. In this case, the WT wake recovers more slowly than in unstable/convective conditions [22]; 2) three wind directions (WD) associated with three different wake patterns; 3) two wind speeds (U) at different WT operational set points.

The stability periods were obtained from the MERRA-2 dataset. As MERRA data are averaged values over a 1/2° × 2/3° tile, the representativeness of the 2.5 E- 49.5 N grid point was assessed by comparing to a bilinear interpolation between the four grid points closest to the WF and the position of the SMV5 WT. No change in the stability periods was found.

Three WDs that produce three different wake patterns were chosen: 1) two wakes inline; 2) two distinct wakes separated 1 D in the crosswise direction; 3) two distinct wakes separated 2 D in the crosswise direction. The WDs considered in each case are limited by the turbulence intensity (I_u). An $I_u = \sigma_U / \overline{U} \approx 0.2$ was determined using information from the meteorological mast. Knowing that the transversal fluctuations are defined as $I_v = 0.75\, I_u$ [23], then the angle of variation is close to $\tan^{-1}(I_v)$, leading to WD bins of ± 8.53°. The historical wind rose (most common WD from the South-West) and the WTs geographical positions were used to determine the center of the *WD* bins. Each post-processed PPI provides the environmental *WD*, where this filter was applied.

Based on the power coefficient of the wind turbine SENVION MM82 (Figure 2) two significant wind speeds were selected, 7 m·s^{-1} and 11 m·s^{-1}, represented by circles on the C_P curve. The standard deviation (σ_U) for the two selected velocities was calculated from the turbulence intensity I_u (σ_U is also presented with error bars in Figure 2). The limits for classifying U data are therefore 7 ± 1.4 m·s^{-1} and 11 ± 2.2 m·s^{-1}. This filter was applied to each single PPI, by extracting the undisturbed wind velocity at hub height.

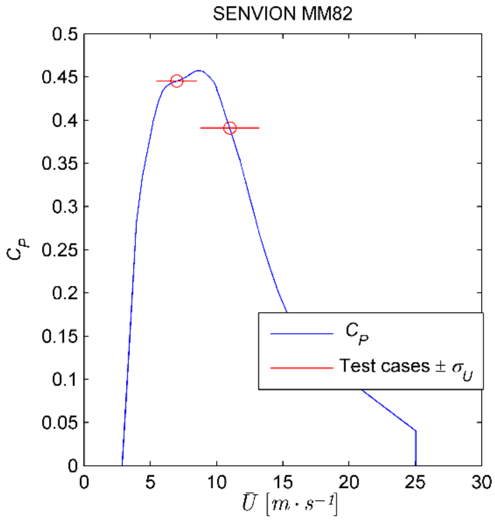

Figure 2. Power coefficient (C_P) of the wind turbine SENVION MM82 as a function of the incoming wind velocity ($\bar{U}$).

3.1. LiDAR data processing

A tool, provided by LEOSPHERE, converts the radial wind velocity measurements into estimated horizontal wind velocities by applying a correction from the cosine of the averaged wind direction. The averaged LiDAR *WD* is retrieved from locations outside of the wake influence.

No measurement was obtained at certain locations due to the lack of environmental aerosols; data at these locations were interpolated. The measurements taken at WT positions were also interpolated. An 80% data availability criterion was established for each PPI scan. If a certain PPI scan had more than 80% of available data, the interpolation was applied, otherwise the PPI was not taken into account. In order to interpolate the measurements, the Laplacian operator was applied over each PPI. Those parts of the PPI that were not in contact with unknown values were dropped and the unknown values were computed by the least squares approach. The measured points were not modified.

In order to validate the *WD* deduced from scanning LiDAR measurements, the alignement of WT wakes with this *WD* was checked. To do so, the inertial coordinates were translated to wind related coordinates, thus each PPI was rotated clockwise according to the *WD* around the ground normal component, to end up with a *WD* orientated system $[X_{WD}, Y_{WD}, Z_{WD}]$. The LiDAR location is defined by $[X_{WD}, Y_{WD}, Z_{WD}]$=(0,0,0). If the *WD* is correctly determined, the rotated PPI should present wakes aligned with the X_{WD} axis. The velocity field was interpolated on a regular grid. It was verified that the instantaneous velocity profile at 4 D downstream had the minimum velocity aligned with the WT hub ± 0.6 D (transversal variation caused by I_v). If the PPI fulfilled this condition, the *WD* is correct and the PPI was taken into account for the statistics.

3.2. Wake tracking

The wake tracking procedure was applied to each PPI (distributed along time, *t*) in the *WD* system, following the procedure proposed in [24]. The wake tracking trajectory is based on the calculation of the wake center coordinate, y_ω, which is a weighted average of the locations Y_{WD} distributed in the crosswise direction $Y_{WD} \pm 0.75$ D from the wind turbine position. The weighting is the exponential of the instantaneous local velocity deficit Du_i, for the N profile points:

$$y_\omega(X_{WD}, t) = \sum_{i=1}^{N} \exp\left(Du_i(X_{WD}, Y_{WD}, t) \times Y_{WD}{}^{i}\right) \Big/ \sum_{i=1}^{N} \exp\left(Du_i(X_{WD}, Y_{WD}, t)\right), \quad (1)$$

where Du_i, is defined as the difference between the local velocity and the maximum velocity at a constant downstream distance (X_{WD}); the Du_i is located at position $Y_{WD}{}^{i}$. This method was designed to work in the far wake area, where the averaged velocity deficit profile is expected to be characterized by only one local minimum.

3.3. Statistical analysis

Since the positions of the wake center in each time step are independent (PPI distributed over 7 months) and the process is considered statistically stationary due to the imposed constraints, all the accessible microstates (captured by each PPI) are equi-probable over a long period of time, and can then be analyzed as an ensemble. The collection of PPIs gives a collection of wake center positions (y_ω) and the statistical analysis was therefore carried out on these wake center positions. The mean and the standard deviation from the wake center location were calculated, then, the relative statistical uncertainty convergence (ϵ) was calculated as a function of the cumulative standard deviation of the wake center position ($C\sigma_{y\omega}$). The statistical uncertainty for the mean wake position is a function of the wake center dispersion and the number of samples, $\epsilon = 1.96 \cdot \sigma_{y\omega} / \sqrt{N}$ where $\sigma_{y\omega}$ is the standard deviation of the wake center position along the number of independent samples N [25]. The factor 1.96 stands for a confidence level of 95%.

4. Results and discussion

Table 1 presents the number of samples treated per case and per PPI elevation. The two digits at the beginning of the case name refer to the *U* and the next three to the *WD*. The minimum number of samples was found in the case 07244, where wakes are parallel, while the maximum number of samples was found in cases 07207 and 11207 (wakes overlapped). When determining the mean wake position, more samples means greater accuracy. There are two facts involved in the determination of the amount of data: one is the recurrence of the wind direction and the other is the availability of quality measurements.

Table 1. Number of PPI-samples (N) available for each case and for each elevation angle. The two digits at the beginning of the case name refer to the *U* and the next three to the *WD*.

		Cases					
		07207	11207	07225	11225	07244	11244
elev.	α_1	284	248	155	255	121	149
	α_2	324	258	167	248	107	152
	α_3	242	184	131	258	105	153

Figure 3 presents the ensemble-averaged velocity fields for α_2, $U = 7 \pm 1.4$ m·s^{-1} and 3 *WD*s (one per panel). In the three cases, the wake development aligns with the *WD*, confirming the ability to determine the *WD* accurately from LiDAR measurements. In the left panel, case 07207, SMV6 and SMV5 are aligned one in front of the other. The SMV6 wake is well identified, presenting a velocity deficit directly downstream of the WT hub. This velocity deficit decreases as the distance from the WT increases. The SMV6 wake is directly in line with turbine SMV5; hence, the downstream velocity of SMV5 has a further decrease that is also noticeable on the plot. On the left side of SMV6 and SMV5 wakes, the signature of the SMV7 wake can be observed. This WT is outside of the measured PPI. The expansion of the SMV7 wake meets with the wake of SMV5 at around [X_{WD} , Y_{WD}]= (900,750). In the panel in the middle, case 07225, the crosswise separation between hubs SMV7 to SMV6 and SMV6 to SMV5 is roughly 3 D and 1 D, respectively. Although SMV7 is outside of the measured PPI, some of its effects are still visible. At around [X_{WD},Y_{WD}]=(1200,500) the SMV7 wake meets the wake of SMV6. The SMV6 wake expansion is very clear. The right limit of the SMV6 wake reaches the position of SMV5, then the SMV5 wake experiences a further velocity decrease; the process of expansion is also noticeable. At the position of SMV4 and upstream, a velocity reduction is measured. One should bear in mind that the measurements at all WT positions were interpolated. In the right panel, case 07244, the crosswise spacing between SMV7 and SMV6 is 3 D and between SMV6 and SMV5 it is 2 D. The velocity decreases just in front of SMV6 and downstream, a further reduction is observed. The velocity deficit remains for a greater distance in comparison with the previous two cases. The SMV6 wake and SMV5 wake have a similar behavior. Upstream of SMV4, the velocity decreases in agreement with SMV5 and SMV6. The specific value of the velocity deficit is beyond of the scope of the present paper.

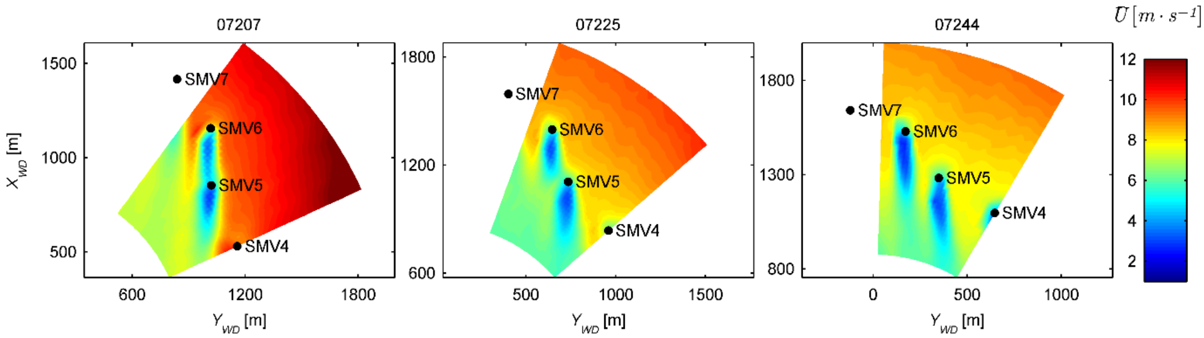

Figure 3. Mean PPI at α_2 = 3.8°, for U = 7 ± 1.4 m· s^{-1} and three WDs ± 8.53°.

In the subsequent plots, the coordinates [X_{WD}, Y_{WD}, Z_{WD}] were nondimensionalised by D and the origin was set to the position of the SMV6 hub.

Figure 4 presents the mean position of the wake center (y_ω) and its standard deviation. The y_ω blue color stands for α_1, the green for α_2 and the red for α_3. SMV6 and SMV5 positions are marked with a black circle and a black square, respectively. The gray area corresponds to the domain where the algorithm for the y_ω computation was applied. Only cases with U = 7 ± 1.4 m·s^{-1} were analyzed, since between the two incoming wind velocities selected (U = 7 m·s^{-1} and U = 11 m·s^{-1}) no remarkable differences were observed.

The first plot of Figure 4 shows the case 07207. The wake center starts at the SMV6 position and is displaced slightly in the -y_{WD}/D direction. This displacement can be attributed to the SMV7 wake, but also to the inability of the method to separate single wake effects. At the SMV5 position, the center starts at hub position for α_1 and α_2. For α_3, the wake center remains aligned with the SMV6 wake. The standard deviation increases with the distance downstream with a noticeable increase after SMV5, due to the sum of the effects of the two wakes. A similar effect was reported by Muller et al. [24].

In the central plot of Figure 4, the SMV6 wake shows the effects of two neighboring wakes interacting in the same domain of calculation. On the -y_{WD}/D side, the SMV7 wake is developed and on the +y_{WD}/D side the SMV5 wake, both at different distances streamwise. Since SMV7 is located at y_{WD}/D ≈ -1, and the wake tracking process weights all the velocities, the center of SMV6 is attracted in this direction. From x_{WD}/D = 3.5, SMV6 y_ω is displaced towards the direction of SMV5 and the standard deviation increases; this deviation diminishes at approximately 3 D downstream of SMV5 and, farther downstream, returns to its initial position (aligned with the WT hub). The SMV5 wake shows a slight displacement towards the direction of SMV6, which is smaller in comparison with SMV6. The standard deviation in SMV5 is similar to case 07207 and higher than SMV6.

The lower plot in Figure 4 presents the case 07244. The y_ω is centered to its respective WT hub. The standard deviation in the SMV6 wake increases with the distance. Following the same curve, 1 D downstream of SMV5 the standard deviation diminishes with the distance. The SMV5 wake shows a higher standard deviation, because the wind is already turbulent (SMV6 wake upstream).

Figure 5 shows the y_ω standard deviation ($\sigma_{y\omega}$) with respect to the location downstream from the source (SMV6 and SMV5 WTs). Each row represents a *WD* range and each column a *U* range. As in the previous plot, blue stands for $\alpha_1 = 2.5°$, green for $\alpha_2 = 3.8°$ and red for $\alpha_3 = 5.2°$; the solid lines represent $\sigma_{y\omega}$ calculated from the collection of wake center positions for SMV6, and the dotted lines SMV5. In most of the cases, from the WT source and up to 1 D downstream, the $\sigma_{y\omega}$ diminishes and then increases with the distance. The interpretation of the results in the near wake should be done carefully, since all the values measured at the WT location were interpolated and because of the limitations of the wake tracking method.

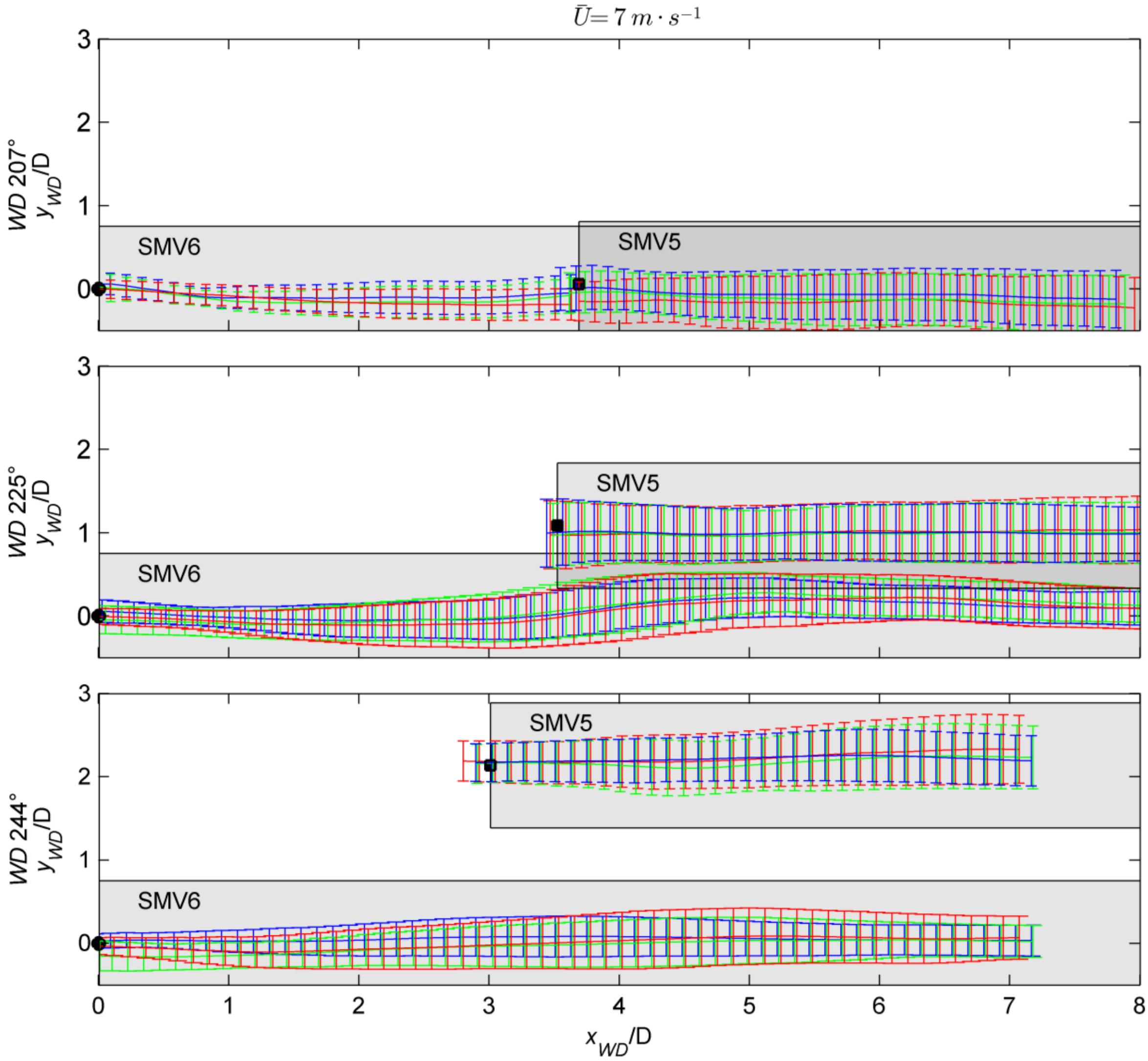

Figure 4. Ensemble average of the wake center locations (y_ω) and its standard deviation ($\pm\, \sigma_{y\omega}$) at different downstream distances. Blue stands for α_1, green for α_2 and red for α_3. SMV6 and SMV5 positions are marked with a black circle and a black square, respectively. The gray area corresponds to y_{WD} /D= WT ± 0.75, the area of wake tracking calculation.

In Figure 5a (case 07207), SMV6's $\sigma_{y\omega}$ increases from 1 D until 3 D downstream and then remains quasi-constant with a value of 0.19. Results from on-field measurements [26] report a value of $\sigma_{y\omega}$ = 0.17 at x/D = 3 for a I_u similar to the one used in the present paper. The SMV5 $\sigma_{y\omega}$ starts with a jump of around 0.05 with respect to the ending of SMV6 and then has a positive slope; this jump is associated to the perturbation due to the WT rotation, and as the flow goes downstream, the accumulation of the wakes of SMV6 and SMV5 is clear since the curve continues to show a positive slope. By increasing the velocity (Figure 5b, case11207), in SMV6 the same initial positive slope is observed, but around 2 D downstream the $\sigma_{y\omega}$ appears to be constant (0.21). In SMV5 the same behavior as in SMV6 is observed but with an increase of $\sigma_{y\omega}$ = 0.15. Note that the trend changes at around 2 D downstream of each WT. This position could mark the end of the near wake and the beginning of the far wake.

In Figure 5c (case 07225), the $\sigma_{y\omega}$ for SMV6 increases from ≈ 0.13 at 1 D downstream up to 0.28 for α_1 or 0.38 for α_3 at approximately 4 D downstream. This difference can be attributed to the limited number of samples; α_3 was calculated with only 131 samples (Table 1). Downstream of SMV6, at around 2 D, there is a change in the tendency; the same position (2 D) and value (0.21) are verified in all the cases. The wake tends to follow the main wind stream, but reaching the position of SMV5, the rotor induces a local modification of the flow and then the wake center is attracted in this direction. In the SMV6 wake, this effect increases the $\sigma_{y\omega}$ at around the position of SMV5. This feature disappears between $x_{WD/D}$= 7 and $x_{WD/D}$=8, where the SMV6 wake reaches the nominal value of 0.2. There is more dispersion in the upper part of the wake that in the lower part. Unfortunately, the number of samples is smaller in the higher elevation. Figure 5d (case 11225) was calculated with almost the same amount of samples per elevation (between 248 and 258). The effect of suction of the wake is observed, increasing the $\sigma_{y\omega}$ value up to 4 D downstream of SMV6 and then decreasing. The higher plane, α_3, experiences more fluctuations. From SMV5, the three elevations give similar results but, with double the number of samples, the congruency between planes is better. The values appear to take into account the turbulence of the wake upstream, reaching almost 0.4.

Figure 5e presents case 07244. A clear difference between PPI elevations is seen, with α_3 the one with a higher $\sigma_{y\omega}$, and also the one with the fewest samples (105). The wake that started upstream shows an increase in the $\sigma_{y\omega}$ up to approximately 1.5 D downstream of the wake that started farther downstream, then there is a decrease in the $\sigma_{y\omega}$. The measurements close to the ground have the same tendency as for case 07225, reaching the nominal value of 0.2 at the end. Case 11244 is presented in Figure 5 f, where SMV6 experiences fluctuations due to disturbance by SMV5. Downstream the value of 0.2 is reached. SMV5 presents a similar positive slope to case 11207 and 3 D downstream it becomes almost constant but with different values between planes. These differences will be explained from Figures 6 to 8.

To conclude, the $\sigma_{y\omega}$ starts at a value between 0.1 and 0.2, providing that upstream there is no other wake disturbing the flow. This value is caused by the environmental I_u. Then, $\sigma_{y\omega}$ diminishes at around 1 D downstream and then increases again. It should be remembered, however, that, as mentioned before, the tracking method might not be suitable for the near wake region. If there are no neighboring wakes, the $\sigma_{y\omega}$ will reach a value of 0.2. If there are neighboring wakes, the second wake will show the sum of effects. In the parallel wakes case, they will influence each other (at least for the transversal distances tested here): the dispersion of the wake that starts first increases up to 1 D downstream of the second wake. The second wake will present the same tendency as the first one but with a greater dispersion. In all the cases at around 2 D downstream, a change in the tendency was observed; this position could mark the end of the near wake and the beginning of the far wake.

Figures 6 to 8 present the cumulative statistical uncertainty (ϵ) convergence of the mean wake center position as a function of the distance downstream from SMV6. In the plots, the vertical axis corresponds to the streamwise position of the wake, while the horizontal axis corresponds to the cumulative statistical uncertainty for a number of samples. In order to facilitate comparison between cases the same length of horizontal axis was used. The three PPI elevations are presented in columns; the first three columns are for U = 7 m·s^{-1} and the last 3 for U = 11 m·s^{-1}.

When the WD is 207° (Figure 6, case 07207), at the closest position to the SMV6 hub (x_{WD}/D =0) the three elevations need only a few samples to converge, as is expected since the source of the wake is fixed and there is no flow modification upstream. Even at the higher elevation, ϵ appears to be constant from a very few samples. At this position the PPI measures above the wake. Moving streamwise, there is more meander and then, to reach convergence, more samples are needed for the three elevations. From SMV6, 60 samples are more than enough to reach a quasi-constant value. The flow leaving SMV6 reaches SMV5, and then in the SMV5 wake, 200 samples are needed to reach the same value of ϵ, due to the turbulence created upstream. In case 11207 in the three elevations, from x_{WD}/D =0, more samples are needed to converge in comparison with case 07207. In α_1 and α_2, a similar convergence with the distance downstream is observed; these two elevations at approximately 150 samples reached the same value of convergence as at 60 samples with U of 7 m·s^{-1}. The higher elevation appears to be more fluctuating but constant along the wake. There is no change in the convergence with the distance downstream. The behavior in SMV5's wake is the sum of SMV6 and SMV5 wakes: more fluctuations are measured and, to reach the same statistical uncertainty, more samples are needed. With the distance downstream, the meandering is increased. Comparing cases 07207 and 11207, it can be seen that the higher the velocity, the larger the number of samples required to reach convergence. It follows, therefore, that the higher elevation also needs more samples to converge (effect of the velocity profile of the atmospheric boundary layer).

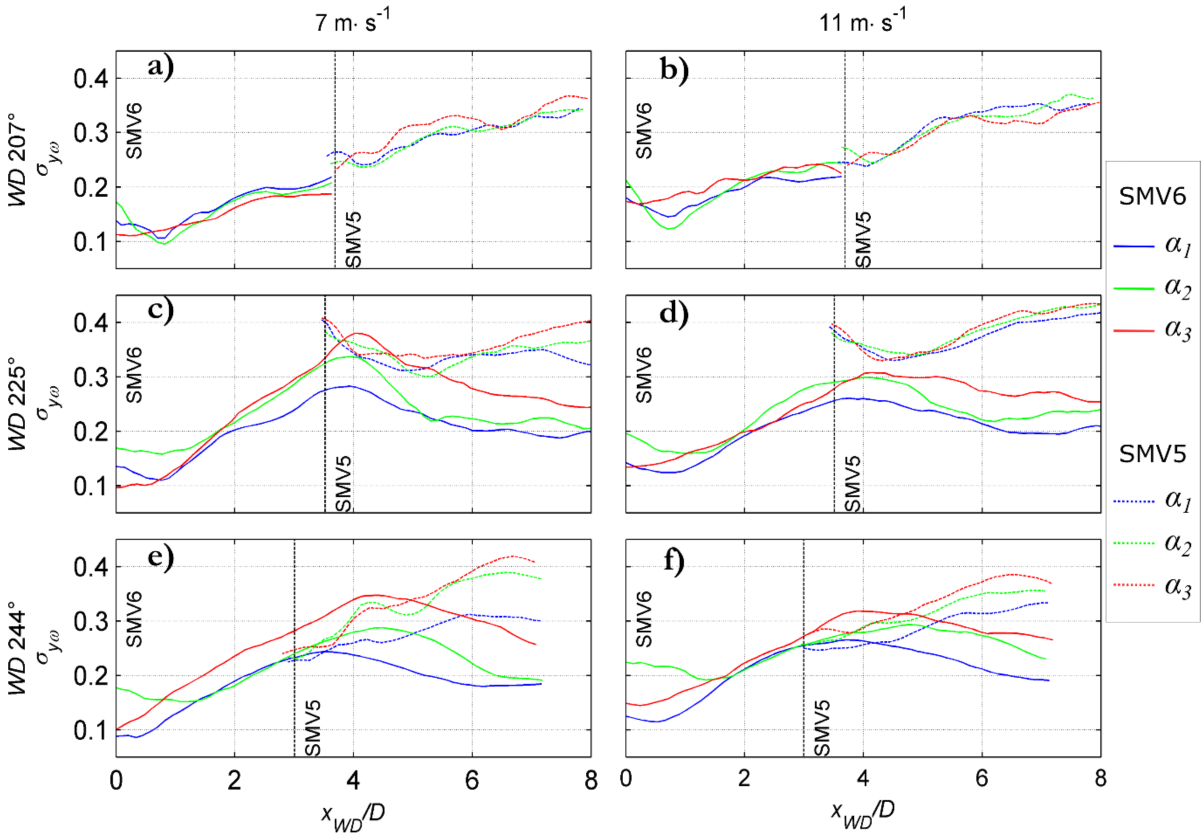

Figure 5. Standard deviation from wake center position ($\sigma_{y\omega}$) as a function of the distance. Blue stands for $\alpha_1 = 2.5°$, green for $\alpha_2 = 3.8°$ and red for $\alpha_3 = 5.2°$. The position x_{WD}/D=0 is the position of SMV6 while the position of SMV5 is referenced with a vertical black dotted line; solid colored lines present the $\sigma_{y\omega}$ for SMV6's wake while the dotted lines correspond to SMV5's wake.

In the cases 07225 and 11225 (Figure 7), SMV6 can be divided into two: the first part, $0 < x_{WD}/D < 3.5$ where the wake behaves in a similar fashion to SMV6 in Figure 6, and the part from $x_{WD}/D = 3.5$ onwards where an influence of SMV5 on SMV6 is seen. In α_1 and α_2 of case 07225, the increase in meandering with the distance is clear, with a break at the position SMV5 and the tendency downstream follows as at the beginning. In α_3 the convergence is slower, mainly in the region of SMV5, where a "hump" appears, and from $x_{WD}/D > 3.5$ the ϵ appears to decay constantly all along the wake with the number of samples. α_1 of case 11225 is similar to the α_3 case 07225, but requires more samples to converge. The α_2 of case 11225 presents the same tendency as α_3 of case 07225 but the "hump" is upstream of SMV5. From 200 samples the ϵ looks constant. In the α_3 of case 11225, more environmental fluctuations are measured and the ϵ value decays slowly. In both cases, the wake on SMV5 is more affected by the turbulence generated by SMV6. Notice that convergence is more difficult to achieve than in the previous case, where SMV5 was directly in line with the wake of SMV6.

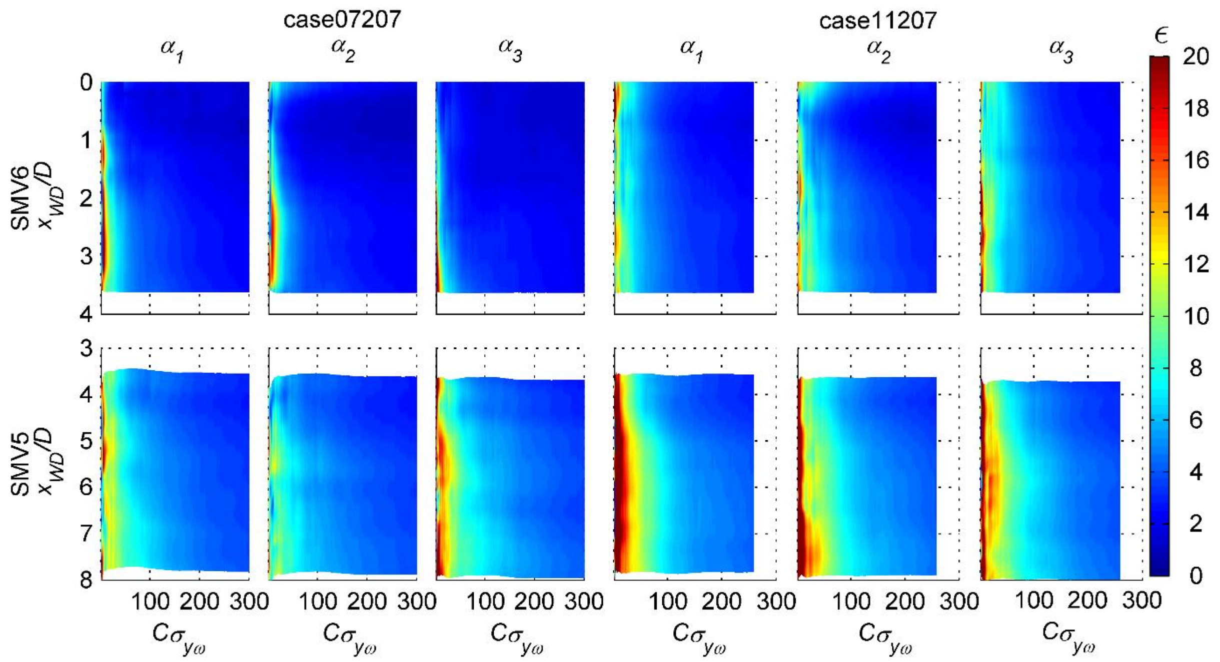

Figure 6. Statistical uncertainty convergence ($\epsilon \times 10^{-2}$ D) as a function of the streamwise position and the cumulative standard deviation of the wake center position ($C\sigma_{y\omega}$). Cases with *WD* = 207°.

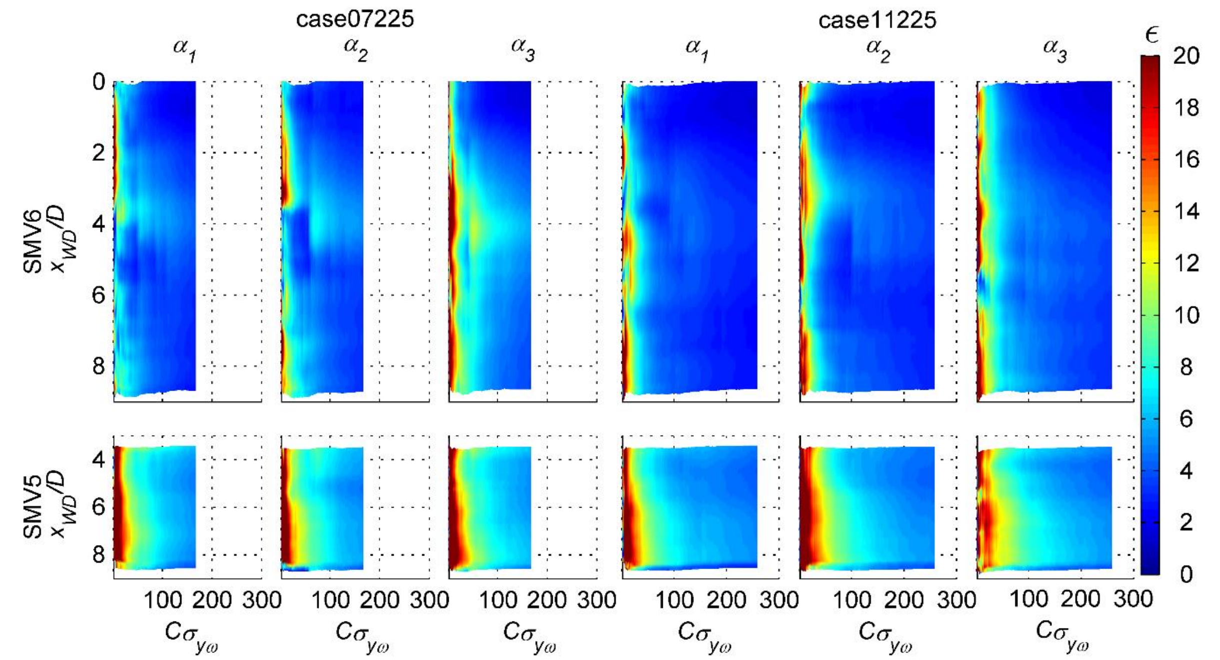

Figure 7. Statistical uncertainty convergence ($\epsilon \times 10^{-2}$ D) as a function of the streamwise position and the cumulative standard deviation of the wake center position ($C\sigma_{y\omega}$). Cases with *WD* 225°.

Figure 8 shows the statistical uncertainty convergence for cases 07244 and 1244. The spacing between hubs' centers is 2 D, even though the influence of SMV5 on SMV6 can be observed. Hence in

SMV6 at x_{WD}/D = 4, more samples are needed to converge. The zone of influence starts approximately 1.5 D upstream of SMV5, making it harder to reach convergence. As the wake propagates downstream (at around 2.5 D downstream of SMV5), the fluctuations are smaller and the error converges faster. The fluctuations appear to be bigger in the higher elevation. Besides the crosswise spacing between WTs, SMV5 receives a turbulent wind and the wind speed does not make any difference. In other words, the statistical uncertainty convergence of SMV5 is similar for the two cases 07244 and 11244.

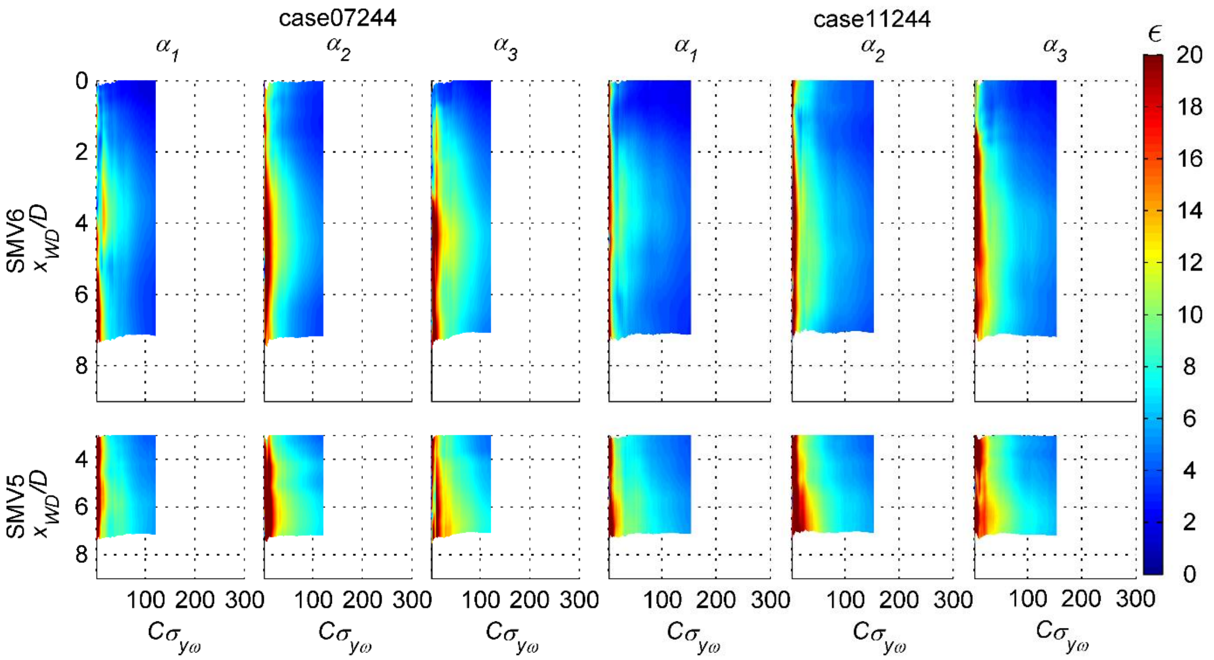

Figure 8. Statistical uncertainty convergence ($\epsilon \times 10^{-2}$ D) as a function of the streamwise position and the cumulative standard deviation of the wake center position ($C\sigma_{y\omega}$). Cases with *WD* 244°.

Table 2 summarizes the statistical uncertainty reached at various positions downstream of SMV6 for each case and for each elevation. As shown in the graphs, the higher values are concentrated where there is interaction between the wake SMV6 and that of SMV5 (shaded in gray). The lower values are reached when the incoming flow is undisturbed (in SMV6 at x_{WD}/D =1 at any elevation). The lateral spacing between the wind turbines does not reduce the fluctuations, and for the cases treated here, a spacing of 2 D produces more fluctuations than if the WT were directly in line with the wake of a WT upstream.

Table 2. Statistical uncertainty ($\epsilon \times 10^{-2}$ D) reached at different distances downstream for the six cases tested. In grey the maximum values at positions of interference of SMV5 on SMV6.

x_{WD}/D		SMV6 Cases						SMV5 Cases					
		07 207	11 207	07 225	11 225	07 244	11 244	07 207	11 207	07 225	11 225	07 244	11 244
α_1	1	1.4	1.9	1.7	1.5	1.7	1.8						
	2	2	2.5	2.7	2.1	3	2.8						
	3.5	2.3	2.7	3.7	3	4.2	4.1						
	4.5			4.3	3.2	4.2	4.1	2.6	3.1	5	4.1	4.7	4.1
	6			3.3	2.7	3.4	3.6	3.3	4.1	5.1	4.5	5.4	4.9
	7			3.1	2.4	3.2	3.1	3.5	4.3	5.3	5	5.5	5.1
α_2	1	1.3	1.8	2.4	2	2.8	3.4						
	2	1.9	2.6	3.1	2.1	3.1	3.2						

	3.5	2.2	3	4.6	3.4	4.5	4.3						
	4.5			4.8	3.7	5.1	4.5	2.6	3	5.3	4.3	6	4.7
	6			3.4	2.9	4.3	4.4	3.4	4	5	4.7	6.6	5.4
	7			3.3	2.7	3.5	3.8	3.5	4.1	5.4	5.1	6.9	5.6
α_3	1	1.4	2.3	2.2	1.8	2.5	2.6						
	2	1.8	2.6	3.8	2.3	3.7	3.3						
	3.5	2	2.9	5.5	3.1	5.1	4.6						
	4.5			5.1	3.7	6.1	5	2.9	3.2	5.1	4	5.5	4.7
	6			4.1	3.4	5.6	4.5	3.6	3.9	5.3	4.7	6.6	5.8
	7			3.9	3.3	5	4.3	3.5	3.9	5.9	5.1	7.5	6

5. Conclusion

In the present study a 7-month measurement campaign, in which a LiDAR ground based system was used, has been analyzed. The target was to analyze the unsteady wake behavior of two wind turbines. The LiDAR measurements were categorized according to atmospheric conditions. To determine the categories, three filter criteria were applied: 1) Neutral atmosphere corresponding to $|L| \geq 1000$. In this case, the WT wake recovers more slowly than in unstable/convective conditions [22]; 2) three wind directions (*WD*) associated with three different wake patterns; 3) two wind speeds (U) at different WT operational set points. The atmospheric stability was extracted from an external resource (MERRA-2 dataset). The *WD* was determined from LiDAR measurements and corroborated by the wake analysis process. In this process, the PPIs were rotated according to the *WD* and the minimum velocity 4 D downstream of the WT hub was verified, hence confirming or not the *WD*. Only PPIs with the right *WD* were used for the statistical process. To each PPI within the same category, a wake tracking procedure was applied and the wake center was determined. In each category the mean and the standard deviation from the wake center were calculated, and the statistical uncertainty was determined.

Analyses showed that the mean wake center position remains streamwise aligned from 1 D downstream onwards. If parallel wakes develop, the centers of both wakes are displaced, moving closer to each other and the fluctuation increases in both wakes. In the cases analyzed here, the maximum crosswise spacing between wind turbines was 2 D. This close spacing affects the neighboring wakes. Since the WTs are also separated streamwise, the effects seen at the wake center depend on its position. The wake center of the first WT deviates towards the second WT and this effect disappears with the distance downstream as the wake aligns with its WT hub origin. The wake that starts second does not deviate from its center but experiences more fluctuations (effect of the wake upstream).

Wake meandering, determined by the standard deviation from the wake's center, increases from 0.1 D at 1 D downstream of the WT location to 0.19 at 3 D downstream. A similar value was found in wind tunnel experiments [26], but this value is conditioned by the nonexistence of neighboring wakes. The statistical uncertainty convergence analysis showed that 120 samples are enough to reach a statistical uncertainty of 8×10^{-2} D for conditions of wakes' interaction, while for non-disturbed incoming wind conditions, the same number of samples provide a statistical uncertainty of 2×10^{-2} D.

Acknowledgements

This research was funded by the French National Research Agency, under the project SMARTEOLE, reference ANR-14-CE05-0034.

References

[1] L.J. Vermeer, J.N. Sørensen, A. Crespo, Wind turbine wake aerodynamics, Prog. Aerosp. Sci. 39 (2003) 467–510. doi:10.1016/S0376-0421(03)00078-2.
[2] M. Bastankhah, F. Porté-Agel, A new analytical model for wind-turbine wakes, Renew. Energy. 70 (2014) 116–123. doi:10.1016/j.renene.2014.01.002.
[3] T.J. Larsen, H.A. Madsen, G.C. Larsen, K.S. Hansen, Validation of the dynamic wake meander model for loads and power production in the Egmond aan Zee wind farm, Wind Energy. 16

(2013) 605–624. doi:10.1002/we.1563.
[4] Y.-T. Wu, F. Porté-Agel, Atmospheric Turbulence Effects on Wind-Turbine Wakes: An LES Study, Energies. 5 (2012) 5340–5362. doi:10.3390/en5125340.
[5] A. Jimenez, A. Crespo, E. Migoya, J. Garcia, Advances in large-eddy simulation of a wind turbine wake, J. Phys. Conf. Ser. 75 (2007) 12041. doi:10.1088/1742-6596/75/1/012041.
[6] G. España, S. Aubrun, S. Loyer, P. Devinant, Wind tunnel study of the wake meandering downstream of a modelled wind turbine as an effect of large scale turbulent eddies, J. Wind Eng. Ind. Aerodyn. 101 (2012) 24–33. doi:10.1016/j.jweia.2011.10.011.
[7] L.P. Chamorro, F. Porté-Agel, A Wind-Tunnel Investigation of Wind-Turbine Wakes: Boundary-Layer Turbulence Effects, Boundary-Layer Meteorol. 132 (2009) 129–149. doi:10.1007/s10546-009-9380-8.
[8] R.J. Barthelmie, S.T. Frandsen, M.N. Nielsen, S.C. Pryor, P.-E. Rethore, H.E. Jørgensen, Modelling and measurements of power losses and turbulence intensity in wind turbine wakes at Middelgrunden offshore wind farm, Wind Energy. 10 (2007) 517–528. doi:10.1002/we.238.
[9] J.K. Lundquist, E.S. Takle, M. Boquet, B. Kosovic, M.E. Rhodes, D. Rajewski, R. Doorenboos, S. Irvin, M.L. Aitken, K. Friedrich, P.T. Quelet, J. Rana, C. St. Martin, B. Vanderwende, W. Rochelle, Lidar observations of interacting wind turbine wakes in an onshore wind farm, Ewea 2014. (2014) 33–36.
[10] V.-M. Kumer, J. Reuder, B. Svardal, C. Sætre, P. Eecen, Characterisation of Single Wind Turbine Wakes with Static and Scanning WINTWEX-W LiDAR Data, Energy Procedia. 80 (2015) 245–254. doi:10.1016/j.egypro.2015.11.428.
[11] G.C. Larsen, E. Machefaux, A. Chougule, Wake meandering under non-neutral atmospheric stability conditions - theory and facts, J. Phys. Conf. Ser. 625 (2015) 12036. http://stacks.iop.org/1742-6596/625/i=1/a=012036.
[12] M.E. Rhodes, J.K. Lundquist, The Effect of Wind-Turbine Wakes on Summertime US Midwest Atmospheric Wind Profiles as Observed with Ground-Based Doppler Lidar, Boundary-Layer Meteorol. 149 (2013) 85–103. doi:10.1007/s10546-013-9834-x.
[13] A. Peña, C.B. Hasager, M. Badger, R.J. Barthelmie, F. Bingöl, J.-P. Cariou, S. Emeis, S.T. Frandsen, M. Harris, I. Karagali, S.E. Larsen, J. Mann, T. Mikkelsen, M. Pitter, S. Pryor, A. Sathe, D. Schlipf, C. Slinger, R. Wagner, Remote Sensing for Wind Energy DTU Wind Energy E-Report Remote Sensing for Wind Energy, 2015.
[14] C.J. Grund, R.M. Banta, J.L. George, J.N. Howell, M.J. Post, R.A. Richer, A.M. Weickmann, High-resolution doppler lidar for boundary layer and cloud research, J. Atmos. Ocean. Technol. 18 (2001) 376–393. doi:10.1175/1520-0426(2001)018<0376:HRDLFB>2.0.CO;2.
[15] S.C. Tucker, C.J. Senff, A.M. Weickmann, W.A. Brewer, R.M. Banta, S.P. Sandberg, D.C. Law, R.M. Hardesty, Doppler Lidar Estimation of Mixing Height Using Turbulence, Shear, and Aerosol Profiles, J. Atmos. Ocean. Technol. 26 (2009) 673–688. doi:10.1175/2008JTECHA1157.1.
[16] J.-J. Trujillo, F. Bingöl, G.C. Larsen, J. Mann, M. Kühn, Light detection and ranging measurements of wake dynamics. Part II: two-dimensional scanning, Wind Energy. 14 (2011) 61–75. doi:10.1002/we.402.
[17] D. Schlipf, D. Trabucchi, O. Bischoff, M. Hofsäß, J. Mann, T. Mikkelsen, A. Rettenmeier, J.-J. Trujillo, M. Kühn, Testing of Frozen Turbulence Hypothesis for Wind Turbine Applications with a Scanning LIDAR System, … Symp. …. 12 (2010) 5410.
[18] S. Aubrun, E. Torres-Garcia, M. Boquet, O. Coupiac, N. Girard, Wind turbine wake tracking and its correlations with wind turbine monitoring sensors. Preliminary results, J. Phys. Conf. Ser. 753 (2016) 32003. doi:10.1088/1742-6596/753/3/032003.
[19] R. Wagner, Comparison test of WLS200S-22 (Final), DTU Wind Energy, Denmark, 2014.
[20] A. Molod, L. Takacs, M. Suarez, J. Bacmeister, Development of the GEOS-5 atmospheric general circulation model: evolution from MERRA to MERRA2, Geosci. Model Dev. 8 (2015) 1339–1356. doi:10.5194/gmd-8-1339-2015.

[21] D. Li, C. Schmitt, C. Meissner, A. Vignaroli, Stability classification for CFD simulations in complex terrain, EWEA Resorce Assess. (2013).
[22] G.V. Iungo, F. Porté-Agel, Volumetric Lidar Scanning of Wind Turbine Wakes under Convective and Neutral Atmospheric Stability Regimes, J. Atmos. Ocean. Technol. 31 (2014) 2035–2048. doi:10.1175/JTECH-D-13-00252.1.
[23] VDI guideline 3783/12, Physical modelling of flow and dispersion processes in the atmospheric boundary layer - Application of wind tunnels, (2000).
[24] Y.-A. Muller, S. Aubrun, C. Masson, Determination of real-time predictors of the wind turbine wake meandering, Exp. Fluids. 56 (2015) 53. doi:10.1007/s00348-015-1923-9.
[25] L.H. Benedict, R.D. Gould, Towards better uncertainty estimates for turbulence statistics, Exp. Fluids. 22 (1996) 129–136. doi:10.1007/s003480050030.
[26] S. Aubrun, T.F. Tchouaké, G. España, G. Larsen, J. Mann, F. Bingöl, Comparison between Wind Tunnel and Field Experiments on Wind Turbine Wake Meandering, in: M. Oberlack, J. Peinke, A. Talamelli, L. Castillo, M. Hölling (Eds.), Prog. Turbul. Wind Energy IV Proc. iTi Conf. Turbul. 2010, Springer Berlin Heidelberg, Berlin, Heidelberg, 2012: pp. 223–226. doi:10.1007/978-3-642-28968-2_47.